# Electrical Capacitance Tomography of Cell Cultures on a CMOS Microelectrode Array

Manar Abdelatty<sup>1</sup>, Joseph Incandela<sup>2</sup>, Kangping Hu<sup>1</sup>, Pushkaraj Joshi<sup>1</sup>, Joseph W. Larkin<sup>2</sup>, Sherief Reda<sup>1</sup>, and Jacob K. Rosenstein<sup>1</sup>

<sup>1</sup>Brown University, Providence, RI, USA <sup>2</sup>Boston University, Boston, MA, USA

Abstract—Electrical capacitance tomography (ECT) can be used to predict information about the interior volume of an object based on measured capacitance at its boundaries. Here, we present a microscale capacitance tomography system with a spatial resolution of 10 microns using an active CMOS microelectrode array. We introduce a deep learning model for reconstructing 3-D volumes of cell cultures using the boundary capacitance measurements acquired from the sensor array, which is trained using a multi-objective loss function that combines a pixel-wise loss function, a distribution-based loss function, and a region-based loss function to improve model's reconstruction accuracy. The multi-objective loss function enhances the model's reconstruction accuracy by 3.2% compared to training only with a pixel-wise loss function. Compared to baseline computational methods, our model achieves an average of 4.6% improvement on the datasets evaluated. We demonstrate our approach on experimental datasets of bacterial biofilms, showcasing the system's ability to resolve microscopic spatial features of cell cultures in three dimensions. Microscale capacitance tomography can be a low-cost, low-power, label-free tool for 3-D imaging of biological samples.

Index Terms—CMOS, biosensor, tomography, inverse problems, deep learning, transposed convolution, microelectrode array

#### I. INTRODUCTION

LECTRICAL capacitance tomography (ECT) is a non-optical imaging technique that reconstructs a cross-sectional image of an area by measuring the mutual capacitance between sensing electrodes placed at its boundary. ECT belongs to a larger family of tomographic imaging techniques, which also includes electrical impedance tomography (EIT) [1]. EIT and ECT exist on a continuum, but whereas EIT may be influenced by both the conductivity and permittivity of the sample, ECT tends to operate at higher frequencies where the permittivity dominates. EIT and ECT have numerous uses measuring volumes containing contrasting materials. Spatial contrasts in conductivity or permittivity are created by changes in the electrical properties within the volume or by movements of fluids or gasses. Applications include monitoring lung volume [2], cancerous tissue imaging [3], [4], neural activity recording [5], [6], [7], and blood flow monitoring [8].

The imaging physics of ECT, in 3-D, are described by the Poisson PDE in Eq. 1, which describes the relationship

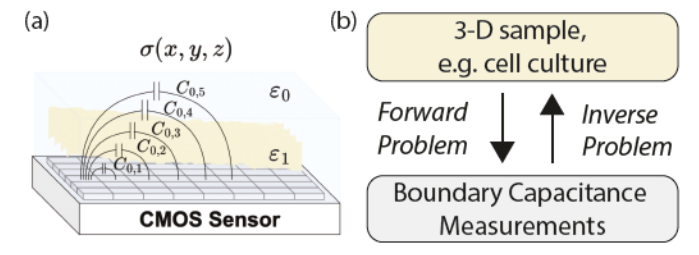


Fig. 1: (a) Capacitance measurements using a planar CMOS microelectrode array underneath the sample of interest. For example,  $\varepsilon_1$  may be the lower dielectric permittivity of a colony of cells growing above the sensor, and  $\varepsilon_0$  may be the higher permittivity of the liquid growth media. (b) Electrical Capacitance Tomography (ECT) aims to computationally solve the inverse problem and predict the 3-D sample geometry from the boundary capacitance measurements.

between the electric potential u(x,y,z) and the interior permittivity distribution  $\sigma(x,y,z)$  [9]. The mapping from the permittivity distribution and the electric potential to the boundary capacitance measurements is described by the integral in Eq. 2, where  $C_{ij}$  is the mutual capacitance between two sensing electrodes i and j,  $V_{ij}$  is the potential difference between the two electrodes, and S is the path enclosing the sensing electrodes. Changes in the internal permittivity affect the electric field distribution, which in turn reflects a change in the measured capacitance at the boundary. The *forward problem* of ECT involves calculating the capacitance measurements based on the permittivity distribution by solving the integral in Eq. 2 [10]. In contrast, the *inverse problem* entails doing the opposite, where the permittivity distribution is estimated based on the boundary capacitance measurements.

$$\nabla \cdot (\sigma(x, y, z) \nabla u(x, y, z)) = 0 \tag{1}$$

$$C_{ij} = -\frac{Q}{V_{ij}} = -\frac{\oint_s \sigma(x, y, z) \nabla u(x, y, z) ds}{u_i - u_j}$$
(2)

The *inverse problem* is inherently challenging as it involves going from the measured capacitance back to the structure of the volume being imaged. This process is both non-linear

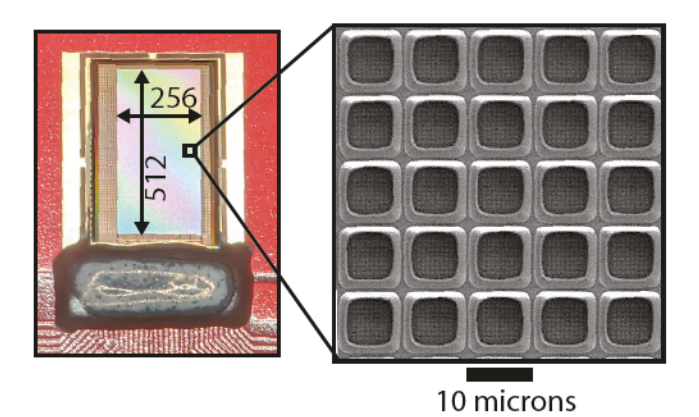


Fig. 2: An image of the CMOS microelectrode array, showing the die photo on the left and a photo of a sub-array of the sensing electrodes on the right. The array has 131, 072 sensing electrodes, each of size  $10 \times 10 \mu m^2$  [18]

and ill-posed, meaning that there are multiple solutions to the problem, and any noise in the measured data can cause significant uncertainties in the estimated cross-sectional permittivity [11]. The inverse problem is traditionally solved by minimizing a least squares objective function with an additional regularization term like the Tikhonov regularization [11] or the total variation [12]. The added regularization prior enforces an additional constraint on the estimated solution to alleviate the ill-posedness of the problem [13]. However, traditional algorithms are not robust to experimental noise, which makes them more susceptible to divergence and often result in low-resolution image reconstructions, in addition to being computationally expensive. Therefore, recent work has focused on using deep learning techniques to solve the inverse problem of ECT, aiming to enhance robustness to noise and obtain higher-quality image reconstructions [14]–[17].

Prior demonstrations of ECT are often implemented using centimeter scale sensing electrodes, which limited their imaging application to macroscopic objects. With appropriate miniaturization of the sensing electrodes, ECT can realize 3-D imaging of micron-scale objects like cell cultures [19]— [24]. Although optical confocal microscopy is often the gold standard for 3-D visualization of living cells, its intense light source and bright illumination can risk damaging the sample through photobleaching and phototoxicity [25]. Additionally, it can be prohibitively expensive for routine use and very slow for observing larger fields of view. Microscale ECT can help address these challenges by offering a non-optical, lowcost imaging technique for visualizing the 3-D structure of cell cultures. There are some early demonstrations of using impedance and capacitance tomography as a non-optical imaging technique of biological samples like tissue cultures [20], stem cells [19], yeast cells [22], and cancer cells [23], [24]. However, these systems use relatively few electrodes with relatively large dimensions, which limits their ability to

resolve finer spatial features and observe larger fields of view. Additionally, they rely on traditional image reconstruction algorithms, which produce only coarse image reconstructions.

To address these challenges, we introduce a microscale electrical capacitance tomography system using a 512 × 256 microelectrode CMOS sensor [18], [26], [27] with a spatial resolution of 10 microns, which is the highest-resolution ECT reported to date. The sensor contains 131,072 sensing electrodes on a  $10 \times 10 \mu m^2$  grid, allowing it to capture 3-D spatial features with a large field of view. The CMOS sensor can be configured to measure the mutual capacitance between any two sensing electrodes in the array. These capacitance measurements are then used as input to the ECT inverse problem to reconstruct the 3-D shapes of the sample above the sensor, as illustrated in Fig. 1. We propose a deep learning model and an enhanced multi-objective training scheme for approximating the ECT inverse operator. In this setup, training data act as a regularization prior to the severely ill-posed inverse problem. Experimental results show that the system is able to accurately predict the 3-D volumes from the CMOS capacitance measurements with a high reconstruction quality.

This work builds on our earlier conference publication [28], which described a microscale electrical capacitance tomography (ECT) system using a CMOS sensor array. In that earlier study, out-of-plane images are reconstructed from a linear array of electrodes. Here, we expand the image reconstruction model to incorporate mutual capacitance measurements from a rectangular grid of electrodes, which provides the model with richer information about the sample's geometry, resulting in more accurate predictions. Using this enhancement, we also expanded the models to predict 3-D volumes instead of predicting vertical 2-D slices. This paper is structured as follows. Section II gives an overview of the capacitance tomography hardware and the different sets of capacitance data acquired from it. Section III describes the architecture of the volume prediction network and the loss function used in training. Section IV discusses the setup for acquiring the experimental dataset used for training and testing. Section V discusses the experimental results obtained on the testing datasets. Finally, in Section VII, we draw conclusions from our findings and suggest potential future research directions.

# II. CAPACITANCE TOMOGRAPHY HARDWARE

The tomography is implemented using capacitance measurements from a planar CMOS microelectrode array, shown in Fig. 2. The sensor design and operating principles are detailed in [18], [27]. The sensor array contains 131,072 sensing electrodes placed on a  $512 \times 256$  rectangular grid with a spatial resolution of  $10\mu m$ . In the mutual capacitance imaging mode, the sensor can measure the capacitance between any two electrodes in the array. Electrode pairs are specified by their spatial separation along both row and column directions. Numerous capacitance data sets can be gathered by adjusting the angles and distances between the sensing electrodes, enabling probing of the sample from multiple angles and yielding

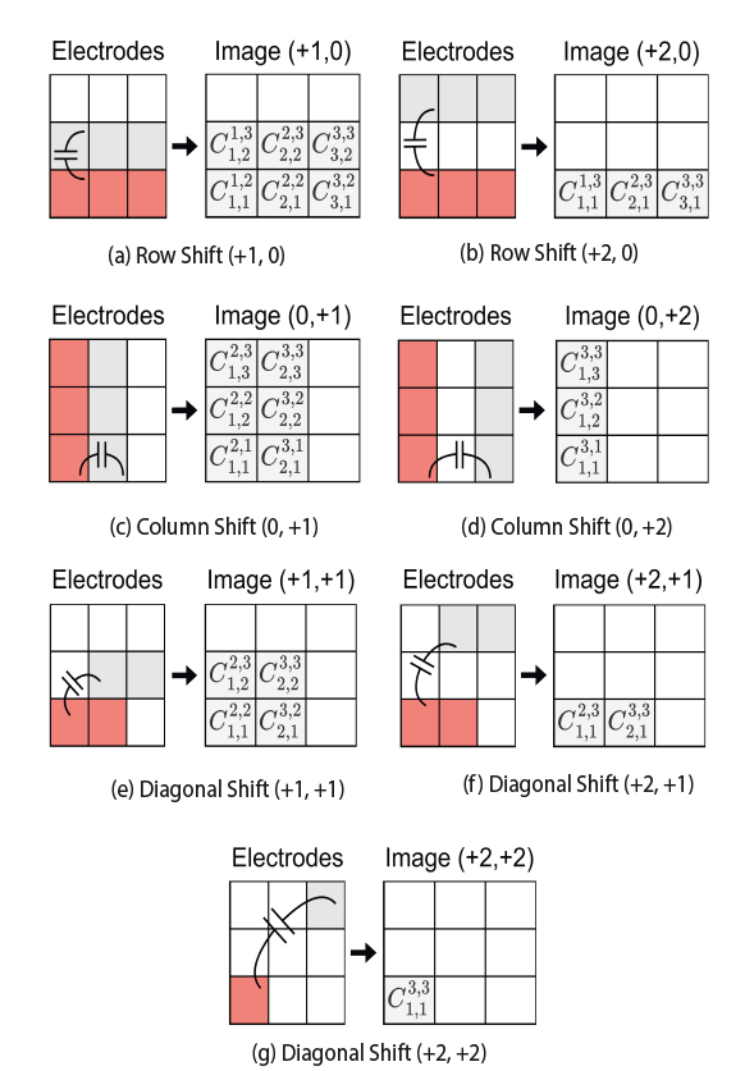


Fig. 3: Mutual capacitance is measured between electrodes at varying spatial offsets. Illustrated above is the capacitance measurements with an (a), (b) offset vector that moves along the rows only,  $(|\delta_i| > 0, \delta_j = 0)$ . (c), (d) offset vector that moves along the columns only,  $(\delta_i = 0, |\delta_j| > 0)$ . (c) offset vector that moves along both rows and columns,  $(|\delta_i| > 0, |\delta_j| > 0)$ .  $C_{i,j}^{k,l}$  represents the capacitance measured between two distinct points within the 2-D electrode array, where (i,j) and (k,l) are the locations of the first and second electrode respectively.

more information about the sample geometry, thickness, and dielectric properties.

The one-sided planar tomography, illustrated in Fig. 1, is performed by placing samples on the chip surface within a gel or liquid electrolyte and measuring the boundary capacitance at varying spatial offsets. The permittivity of the cell culture  $(\varepsilon_1)$  is typically different from the permittivity of the surrounding electrolyte  $(\varepsilon_0)$ . The capacitance value  $C_{ij}$  is the result of fringing electric fields that traverse through the sample. The measured capacitances are primarily influenced by the

volume of the sample within tens of microns of the chip surface, which also constrains the effective sensing depth and effective tomography depth. The capacitance measurements are also modestly affected by the sample's ionic conductance and temperature, so it is helpful to hold these parameters constant between the training and test data.

Fig. 3 illustrates the different sets of capacitance measurements acquired from the CMOS sensor by varying the spatial distance between the sensing electrodes. The spatial distance is specified by an offset vector  $(\delta_i, \delta_j)$ , where  $\delta_i$  indicates the distance between the sensing electrodes in the row direction and  $\delta_i$  indicates the distance in the column direction. The measured capacitance can be categorized into three different datasets: (1) row shift data, where the offset vector only moves along the rows (2) column shift data, where the offset vector only moves along the columns; and (3) diagonal shift data, where the offset vector traverses both the rows and columns. Fig. (3a, 3b) illustrate the row shift measurements with  $|\delta_i| > 0$  and  $\delta_i = 0$ . Conversely, the column shift data, illustrated in Fig. (3c, 3d) has an offset vector with  $\delta_i = 0$ and  $|\delta_i| > 0$ . The diagonal shift data traverses the rows and columns simultaneously with  $|\delta_i|, |\delta_j| > 0$ , as illustrated in Fig. (3e-3g). Measurements at longer offset vectors can add more depth information as the electric field penetrates deeper into the sample. However, the mutual capacitance also decreases with distance, and thus only measurements with  $|\delta_i - \delta_i| < 5$  are considered. These capacitance measurements are input to the inverse problem to reconstruct the 3-D shape of the sample above the sensor.

## III. SHAPE RECONSTRUCTION NETWORK

Deep neural networks (DNNs) are powerful and flexible function approximators, capable of accurately representing complex relationships within data. Different DNN architecture are presented in [15]–[17] for solving the ECT inverse problem. In this setup, training data act as a regularization prior for the severely ill-posed inverse problem. However, these studies mainly focus on predicting 2-D images rather than 3-D shapes. In our application, we need to resolve 3-D shapes directly from the input capacitance measurements. We propose a 3-D architecture based on transposed convolution that takes as an input a matrix of capacitance measurements and outputs the predicted 3-D geometry of the cell culture.

## A. Architecture

Fig. 4 illustrates the architecture of the shape reconstruction network. The network takes as an input a matrix of boundary capacitance measurements with dimensions  $m \times n \times r$ , where m represents the number of electrodes along the rows, n the number of electrodes along the columns, and r the maximum number of spatial offsets considered when measuring the capacitance. The input matrix is reshaped to  $num\_meas \times 1 \times 1 \times d$ , where  $num\_meas$  represents the total number of capacitance measurements in the matrix and d represents the target depth for the reconstructed 3-D shape. The reshaped matrix is then up-sampled through five transposed convolution blocks until

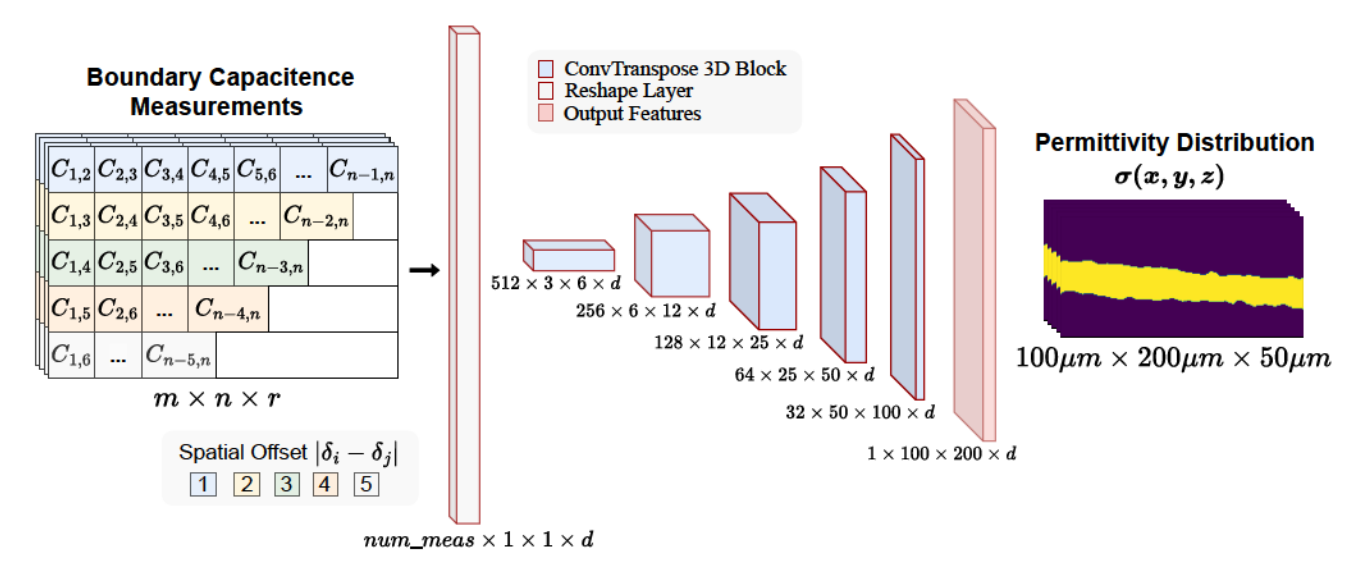


Fig. 4: Shape reconstruction network, based on 3-D transposed convolution. The input is a matrix of pairwise capacitance measurements acquired from the CMOS sensor. The output is a  $50\mu m \times 200\mu m \times 100 \mu m$  cross-sectional volume that represents the 3-D spatial permittivity distribution  $\sigma(x, y, z)$  of the sample above the sensor.

we resolve the dimension of the predicted 3-D volume above the sensor. The reconstructed 3-D volume spatial dimension is set to  $(H, W, C) = 100\mu m \times 200\mu m \times 50\mu m$ .

The network mainly consists of five transposed convolution blocks that iteratively up-sample the input capacitance measurements. Each block contains a 3-D transposed convolution layer, 3-D batch normalization, and a ReLU activation function, except for the final block, which contains a sigmoid activation to constrain the predicted output values within a [0,1] range. The transposed convolution layer contains a 3-D learnable kernel that up-samples the input feature map [29]. The 3-D batch normalization layer ensures training stability and speeds up convergence by normalizing the layer inputs [30]. The ReLU activation ensures that the network can learn the non-linear relationship between the input capacitance and the 3-D permittivity distribution. Additionally, the final output of each block is augmented with a residual connection from the block's input by a  $1 \times 1$  transposed convolution layer to provide an alternative path for the flow of information.

## B. Loss and Training

The loss function is important in deep learning algorithms as it guides the model during the training process and defines the training objective. Choosing the appropriate loss function is essential for ensuring the model's convergence during training. A significant challenge arises from class imbalance in the permittivity maps, where foreground pixels occupy a smaller region than background pixels. Zhu [16] pointed out that distribution-based loss functions like focal loss can mitigate issues caused by the class-imbalance problem. However, studies on medical image segmentation tasks have demonstrated that region-based losses and compound losses perform better than distribution-based losses [31]. Therefore, we propose a compound loss function (Eq. 3) which combines

multiple objectives that focus mainly on the foreground pixels to help address the class-imbalance problem. Here,  $\sigma$  defines the confocal ground truth 3-D volume, while  $\hat{\sigma}$  defines the predicted 3-D volume. The weighting parameters,  $(\lambda_1, \lambda_2, \lambda_3)$ , define the contribution of each loss objective and are optimized during the training process.

$$L(\sigma, \hat{\sigma}) = \lambda_1 L_{\text{SmoothL1}}(\sigma, \hat{\sigma}) + \lambda_2 L_{\text{Focal Loss}}(\sigma, \hat{\sigma}) + \lambda_3 L_{\text{Dice Loss}}(\sigma, \hat{\sigma})$$
(3)

The first objective in our compound loss function is the smooth L1 loss. This pixel-to-pixel loss function uniformly addresses errors in the background and foreground pixels. Defined as a piecewise function in Eq. 4, the smooth 11 loss iterates over all voxels in the predicted and ground truth 3-D volume. It applies a quadratic term for minor errors and transitions to a linear term for more substantial errors, making it less sensitive to outliers compared to the mean-squared error (MSE) loss. The final loss value is the mean of the error across all voxels. It is mainly used for small-scale refinements and enhancing overall pixel accuracy.

$$\begin{split} L_{\text{Smooth L1}}(\sigma, \hat{\sigma}) &= \frac{1}{N} \sum_{i}^{N} SmoothL1(\sigma_{i}, \hat{\sigma_{i}}) \\ &= \frac{1}{N} \sum_{i}^{N} \begin{cases} (\sigma_{i} - \hat{\sigma}_{i})^{2} & \text{if } |\sigma_{i} - \hat{\sigma_{i}}| < 0.5 \\ |\sigma_{i} - \hat{\sigma_{i}}| & \text{otherwise} \end{cases} \end{split} \tag{4}$$

The second objective is the focal loss [32], which is an enhanced cross-entropy loss function designed to address the class-imbalance problem by modifying the loss value with a scaling factor. The focal loss is defined in Eq. 5, where  $p_t$  is the probability of ground truth predictions, calculated by passing

the model's output through a softmax layer. The loss down-scaling is managed by the modulating factor  $\alpha(1-p_t)^{\gamma}$ , which down-weights the loss value for well-predicted examples, thus helping the model focus more on hard-to-predict examples. The focusing parameter  $\gamma$  is used to control the rate of down-weighting easy-to-predict examples, while  $\alpha_t$  is used to control the weighting factor for the loss across the two classes in the predictions, which are the background and foreground pixels.

$$L_{\text{Focal Loss}}(p_t) = -\alpha_t (1 - p_t)^{\gamma} \log(p_t) \tag{5}$$

The third objective is the dice loss function [33], which is a region-based loss function that maximizes the region overlap between the ground truth and the predictions. This encourages the model to produce more spatially aligned predictions and increases edge smoothness. It also helps address the class imbalance issue by focusing on the overlap region rather than each pixel independently. Eq. 6 defines the dice loss function.

$$L_{\text{Dice Loss}}(\sigma, \hat{\sigma}) = 1 - \frac{2|\sigma \cap \hat{\sigma}|}{|\sigma| \cup |\hat{\sigma}|}$$
 (6)

#### IV. EXPERIMENTAL DATASET

The quality of the training dataset is critical to the accuracy of the approximation to the ECT inverse operator. To train the networks, we designed experiments that would allow ECT measurements of a cell culture in addition to 3-D optical confocal microscopy of the same sample. Data from the CMOS sensor serve as the boundary capacitance measurements, and the confocal microscope data is used as the ground truth reference.

The experimental setup incorporating both ECT and confocal microscopy is illustrated in Fig. 5. An  $\sim 800~\mu m$  deep well was created with a stack of four  $25~\mu L$  adhesive chambers (Gene Frame, Thermo Scientific) surrounding the CMOS sensor. A 1% agarose MSGG pad was prepared to match the well depth and sensor area. Wild-type *B. subtilis* cells (NCIB3610) were grown aerobically in a shaken 3mL culture of MSGG at 37°C, until they reached mid-exponential growth phase ( $\sim 1.5$ -2 hours). The liquid culture was then inoculated onto the agarose pad and grown into mature biofilms over a period of 12-16 hours at 30°C. The inoculation concentrations and growth times were varied to produce biofilms of varying surface roughness and thickness.

The CMOS surface was primed with methanol to improve wetting, and then exchanged with phosphate buffered saline (PBS). The agarose pad with a mature biofilm was held on a 1cm<sup>2</sup> polymer coverslip (Uncoated Polymer, Ibidi), and placed in contact with the CMOS sensor. The edges of the sample were then sealed with silicone elastomer (Ecoflex 5) before being mounted on a confocal microscope (Stellaris 5, Leica). The fluorescent dye Thioflavin T (ex/em: 450nm/492nm [34]) was added to both the agarose pad and PBS allowing cells to be visualized.

We acquired a set of mutual capacitance images with varying offset vectors, in addition to a 3-D stack of confocal images spanning the full XY sensor area and a Z-axis

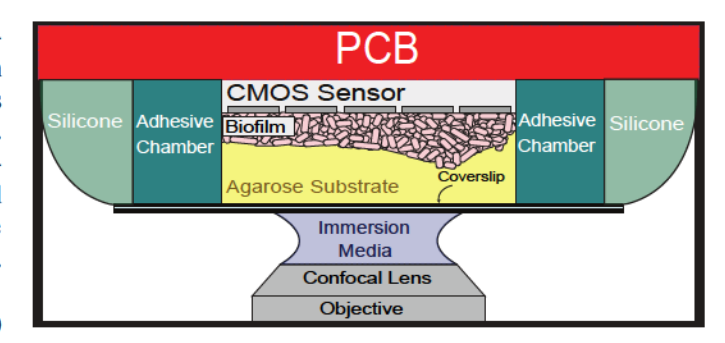


Fig. 5: Experimental dataset acquisition setup, where biofilm samples were mounted to allow both ECT measurements from the CMOS sensor as well as 3-D optical images from a confocal microscope.

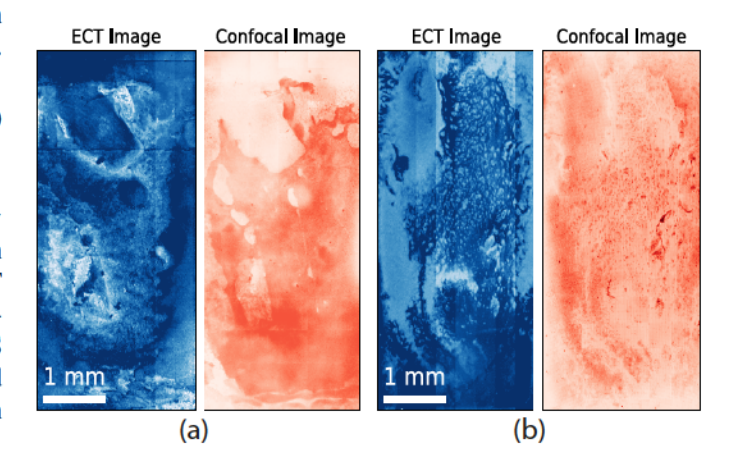


Fig. 6: Two experimental datasets with *B. subtilis* biofilms on the CMOS sensor array. Each sample is shown with one mutual capacitance image (left, measured using a spatial offset of 1) and the confocal max projection (right).

depth of 150  $\mu m$  taken with a 25x/0.95NA water immersion objective (Leica HC Fluotar). Fig. 6 shows ECT images obtained at an offset vector of  $(\delta_i, \delta_j) = (0, +1)$ , alongside the maximum projection of the confocal 3-D stack on the XY plane. The dataset was partitioned into  $100 \, \mu m \times 200 \, \mu m \times 50 \, \mu m$  smaller volumes, and their corresponding boundary capacitance measurements. This yielded 1,310 capacitance and confocal pairs that were split into 80% training and 20% for testing and validation. To circumvent training data scarcity, we augmented it by sampling volumes with an overlapping stride.

#### V. EXPERIMENTAL RESULTS

## A. 3-D Shape Reconstructions

The 3-D volume reconstruction from one local partition incorporates capacitance measurements from a  $20 \times 5$  array of electrodes. Fig. 7 shows the reconstructed 3-D volumes from the CMOS capacitance measurements on four examples from the testing dataset. The results demonstrate the system's ability to resolve the cell culture's geometry in three dimensions.

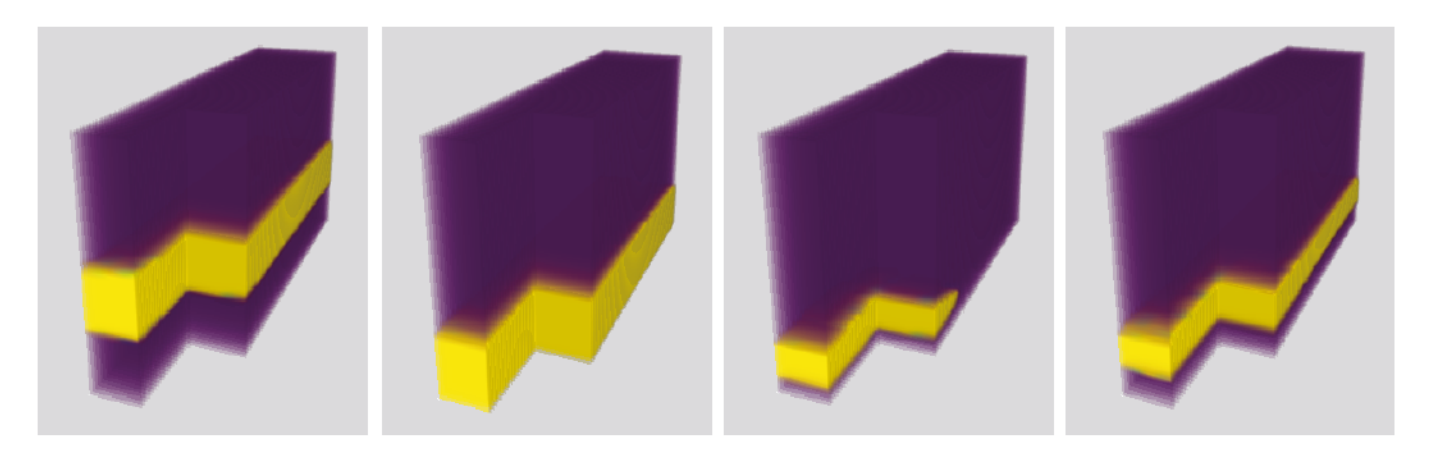


Fig. 7: Reconstructed 3-D volumes of several portions of the B. subtilis biofilm.

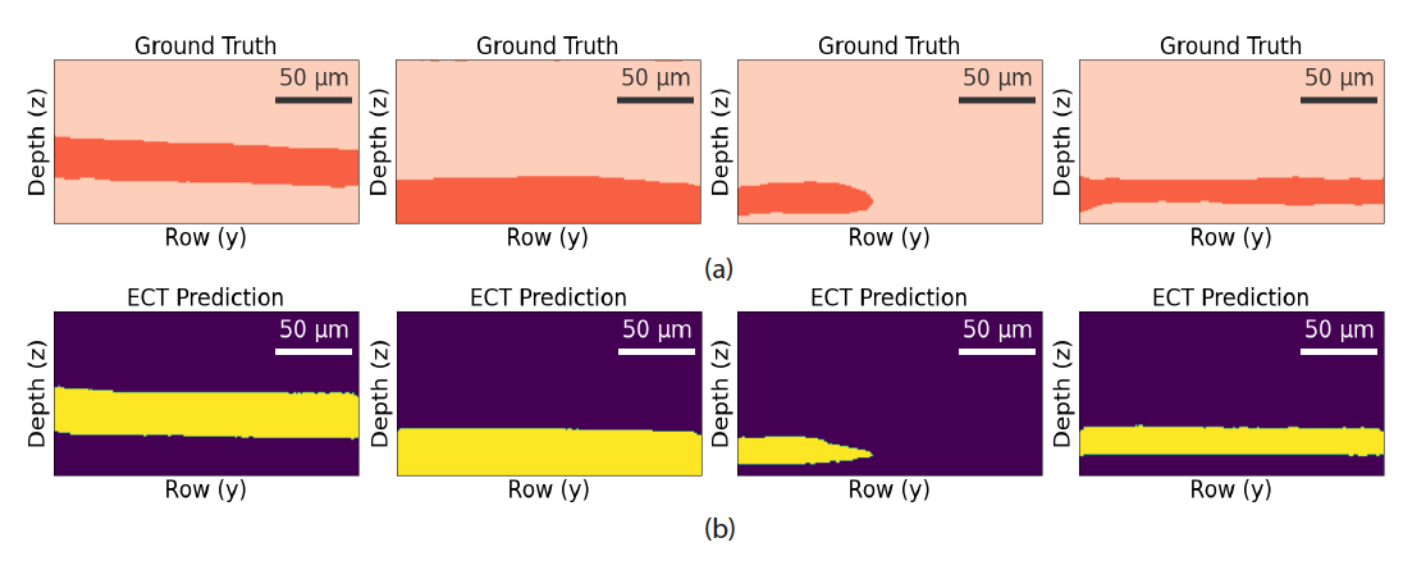


Fig. 8: Maximum projection of the reconstructed 3-D volumes on the YZ plane. (a) Confocal microscopy ground truth max projection. (b) ECT model prediction max projection.

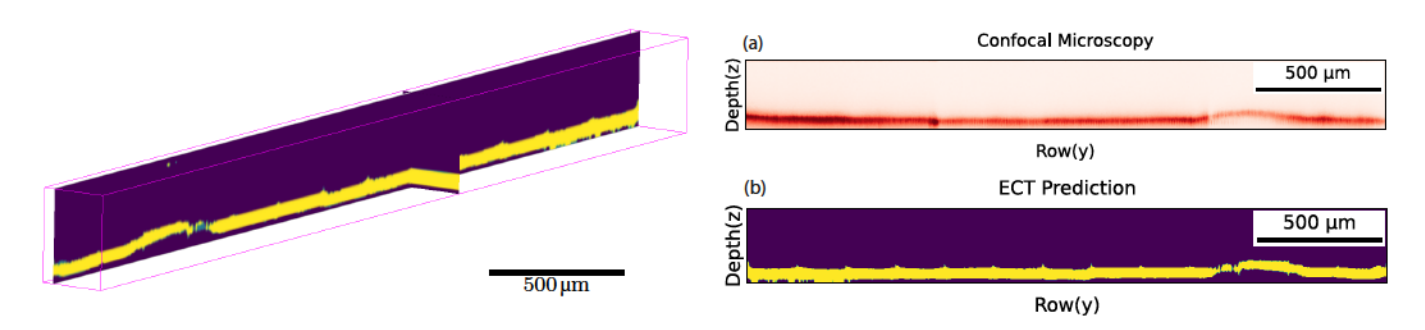


Fig. 9: Reconstruction of a larger-scale cross-sectional 3-D volume of a *B. subtilis* biofilm spanning 2.8 mm. Model predictions were stitched together from fourteen  $200 \,\mu\text{m}$  volumes.

Additionally, Fig. 8 compares the maximum projection of the reconstructed volumes to the confocal microscopy ground truth along slices in the YZ plane, showing the system's ability to accurately predict the biofilm sample's geometry, thickness,

Fig. 10: Max projection of reconstruction of a larger-scale cross-sectional 3-D volume of a *B. subtilis* biofilm spanning 2.8 mm. (a) Confocal ground truth. (b) Model prediction, stitched together from fourteen  $200 \,\mu\mathrm{m}$  volumes.

and location.

The 3-D reconstructions were performed independently

TABLE I: Quantitative analysis comparing previous studies with the use of the microsphere  $(\Omega_1)$  and biofilm  $(\Omega_2, \Omega_3)$  2-D testing datasets, along with quantitative results from the 3-D shape reconstruction based on the 3-D biofilm testing dataset.

		Dataset	MSE ↓	SSIM ↑	PSNR ↑	CC ↑	IoU ↑	MPA ↑
		$\Omega_1$	0.315	0.041	5.015	0.208	0.488	0.538
2-D	Iterated-Tikhonov	$\Omega_2$	0.115	0.569	9.395	0.171	0.362	0.553
		$\Omega_3$	0.127	0.576	8.949	0.048	0.257	0.511
		$\Omega_1$	0.027	0.423	15.73	0.238	0.485	0.952
	Fully-connected auto-encoder (FNN-AE) [15]	$\Omega_2$	0.145	0.678	8.360	0.447	0.591	0.854
		$\Omega_3$	0.112	0.845	9.509	0.540	0.515	0.888
	FNN+CNN autoencoder (FNN+CNN-AE) [16]	$\Omega_1$	0.018	0.931	17.452	0.679	0.766	0.982
		$\Omega_2$	0.105	0.700	9.773	0.649	0.719	0.895
		$\Omega_3$	0.060	0.853	12.221	0.710	0.759	0.940
	self-attention encoder+UNet (self-atnn+UNet) [17]	$\Omega_1$	0.007	0.970	21.296	0.874	0.875	0.993
		$\Omega_2$	0.071	0.785	11.479	0.694	0.775	0.929
		$\Omega_3$	0.050	0.879	13.030	0.734	0.748	0.950
	TCNN+Multi-objective-loss TCNN+MOL (Ours)	$\Omega_1$	0.005	0.975	23.053	0.911	0.915	0.995
		$\Omega_2$	0.057	0.799	12.473	0.781	0.827	0.943
	-	$\Omega_3$	0.043	0.882	13.658	0.722	0.800	0.957
2 D	TONN Multi chicative loss TONN MOL (Owns)	$\Omega_2$	0.048	0.859	13.230	0.806	0.829	0.952
3-D	TCNN+Multi-objective-loss TCNN+MOL (Ours)	$\Omega_3$	0.033	0.893	14.878	0.772	0.843	0.967

on smaller volumes, but by stitching together multiple predictions, we can reconstruct larger sample volumes. Fig. 9 shows the orthogonal slices of the model's predictions over a 2.8mm length, demonstrating the system's ability to resolve millimeter-scale spatial features in cell cultures. Comparison with the confocal microscopy ground truth in Fig. 10 demonstrates a good correspondence between the 2-D max projection of the model prediction and the ground truth confocal microscopy.

## B. Reconstruction Quality

In evaluating the model's reconstruction quality, we utilize a comprehensive set of metrics that assess the similarity between the predicted 3-D shapes and confocal ground truth. Mean Squared Error (MSE) is a fundamental measure that quantifies the average squared difference between the ground truth and reconstructed 3-D shapes. Perceptual metrics that include the Structural Similarity Index Measure (SSIM) [35], Peak Signalto-Noise Ratio (PSNR), and Cross-Correlation (CC) are used to evaluate the visual similarity between the ground truth and the reconstructed 3-D shapes. Additionally, Intersection Over Union (IoU) is used to assess the overlap accuracy of the reconstructions and the ground truth. Lastly, Mean Pixel Accuracy (MPA) calculates the average proportion of correctly predicted pixels, providing a straightforward metric for evaluating overall pixel-level accuracy. Table I shows the 3-D shape reconstruction quality on the biofilm experimental data testing datasets. Here,  $\Omega_2$  refers to the biofilm data in Fig. 6a, and  $\Omega_3$  refers to the biofilm data in Fig. 6b. As measured by the IoU metric, the model achieves a prediction accuracy

of 82.9% and 84.5% on the  $\Omega_2$  and  $\Omega_3$  testing datasets, respectively.

Additionally, we compare the model's reconstruction quality with four baseline methods. The first baseline is the iterated Tikhonov, which solves the ECT inverse problem by iteratively searching for the estimated 3-D permittivity volume that aligns with the input capacitance measurements, employing the Gauss-Newton algorithm for this optimization process. The second baseline is the Fully connected Neural Network Autoencoder (FNN-AE) introduced in [15], which consists of two fully connected neural networks, one for solving the forward problem and the other for solving the inverse problem, co-trained simultaneously using the mean square error (MSE) loss function. The third baseline is the permittivity value prediction network presented in [16], which also incorporates two FNNs for simultaneous resolution of the forward and inverse problems, complemented by a postprocessing convolutional auto-encoder (CNN-AE) designed to enhance the quality of the inverse FNN predictions. The fourth baseline is a UNet-based architecture, presented in [17], which incorporates a self-attention encoder for processing the input capacitance measurements followed by a UNet network to predict the permittivity distribution. By benchmarking against these models, we highlight that choosing the appropriate loss function yields more significant improvements than those achieved by adding complexities to the network architecture.

Since the referenced baselines are designed to predict 2-D cross-sectional images instead of 3-D shapes, we evaluate them alongside our proposed model in a two-dimensional setting. Table I shows the comparison results for the 2-D case

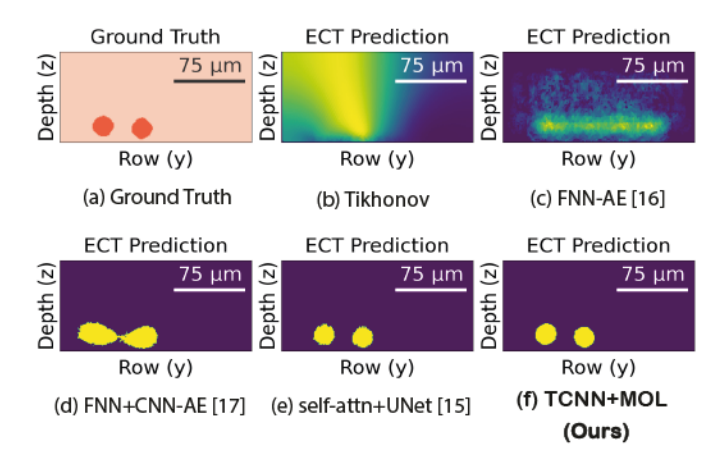


Fig. 11: Qualitative comparison to prior algorithms, using a scene of two microspheres simulated using pyEIT [36].

for three different datasets. The first dataset  $(\Omega_1)$  is a synthetic dataset of microsphere beads generated from pyEIT [36]. The remaining two datasets,  $(\Omega_2 \text{ and } \Omega_3)$ , are the experimental biofilm datasets shown in Fig. 6. The comparisons show that our model consistently improves the prediction accuracy over the referenced benchmarks across all datasets.

We also present a visual comparison between the four baselines and our model reconstructions on one example from the microsphere dataset in Fig. 11, where the ground truth cross-sectional image contains two beads in close proximity. The Tikhonov algorithm gives an accurate estimate of where the beads are located. However, it fails to recognize the presence of two distinct beads and struggles with predicting sharp boundaries between them. This limitation is attributed to the Tikhonov penalty, which favors smooth and continuous solutions, leading to the blurring of edges [37]. The FNN-AE also fails to predict two distinct beads, primarily because fully connected layers are unsuitable for the image prediction task. While the CNN-autoencoder improves the image prediction of the fully connected layer, the resulting FNN+CNN-AE prediction smears out the two beads, muddying the sharp boundary between them. The self-attn+UNet model significantly improves image reconstruction, mainly because the UNet model is well-suited for the image reconstruction task. However, the predicted beads have non-smooth boundaries, mainly because the model is trained with the MSE loss function, which leads to less uncertainty in the predictions around the edges [38]. By incorporating a composite loss function, our proposed model TCNN+MOL prediction accurately captures the locations and the number of beads and improves the smoothness of the edges.

In Fig. 12, we present a similar comparison on one sample from the experimental biofilm dataset. The Tikhonov algorithm fails to converge while solving the optimization objective, mainly due to the experimental noise in the capacitance measurement collected from the CMOS sensor. The FNN-AE falls into a local minimum, favoring predicting a continuous biofilm near the chip surface, a typical pattern in the dataset.

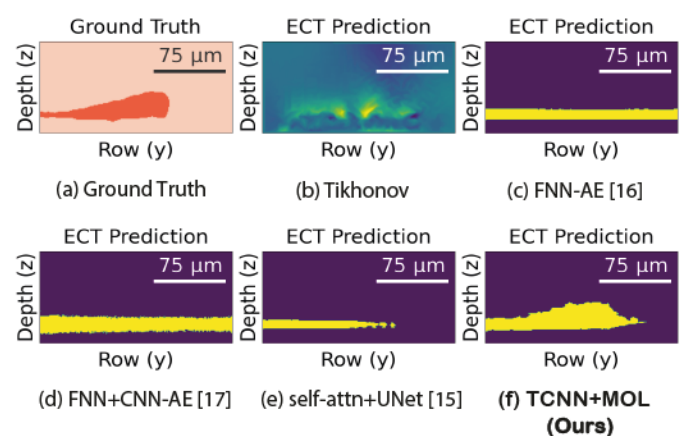


Fig. 12: Qualitative comparison to prior algorithms, using one sample vertical cross-section from the biofilm testing dataset.

The FNN+CNN-AE also fails to predict discontinuity in the biofilm. The self-attn+UNet model can predict the discontinuity in biofilm but underestimates its thickness. Our proposed TCNN+MOL model accurately captures the biofilm's thickness, location, and overall shape, highlighting the importance of incorporating different objectives in the loss function during training to address the class imbalance problem.

#### C. Ablation Study

To understand the contribution of the different capacitance measurements to the model's reconstruction accuracy, we conduct an ablation study on training the model with different combinations of the input capacitance measurements. Our model was initially trained on the three different sets of capacitance measurements: row shift, column shift, and diagonal shift, which were consistently ablated in this experiment to assess their impact on the model's reconstruction accuracy. Table II shows the IoU value when training the model for 20 epochs with different combinations of the input capacitance measurements. Training only with the row shift data achieves a 6% accuracy increase compared to using column shift or diagonal shift data alone or in combination. This suggests that the

TABLE II: Contribution of the input capacitance measurements to the reconstruction accuracy.

Row Shift	Column Shift	Diagonal Shift	IoU
✓			0.7713
	✓		0.7174
		$\checkmark$	0.7120
✓	$\checkmark$		0.7820
	✓	$\checkmark$	0.7137
$\checkmark$		$\checkmark$	0.7845
$\checkmark$	✓	✓	0.7870

TABLE III: Comparison to prior planar electrical tomography systems, including both capacitance and impedance tomography.

	[17]	[23]	[24]	[20]	[22]	[19]	This Work
Imaging Domain	Circular	Planar	Planar	Planar	Planar	Planar	Planar
Domain Shape	2-D	3-D	3-D	3-D	3-D	2-D	3-D
Boundary Measurement	Capacitance	Impedance	Impedance	Impedance	Capacitance	Impedance	Capacitance
Reconstruction Algorithm	self-attn+UNet	Laplacian Regularization	Total Variation	Projected Image Reconstruction Algorithm [39]	Linear Back-projection	Gauss-Newton Least Squares	TCNN+MOL
Imaging Application	Cryogenic Fluids	Cancer Cells	Cancer Cells	Tissue Culture	Yeast cells	Stem Cells	Bacterial biofilms
Electrode Arrangement	Ring	Circular Grid	Circular Grid	Cuboid Grid	Circular Grid	Rectangular Grid	Rectangular Grid
Electrode Size	cm scale	mm scale (1.2x0.6 mm <sup>2</sup> )	mm scale (0.071 mm <sup>2</sup> )	mm scale (0.7854 mm <sup>2</sup> )	mm scale (1.4x0.8mm <sup>2</sup> )	$\mu m$ scale $(5\mu m \times 4mm)$	μ <b>m</b> scale (10x10μ <b>m</b> <sup>2</sup> )
Array Size	8 electrodes	16 electrodes	17 electrodes	360 electrodes	32 electrodes	16 electrodes	100 electrodes (each prediction) 131,072 electrodes (whole array)

TABLE IV: Impact of the loss function choice on the reconstruction accuracy.

Loss	IoU
L <sub>Smooth L1</sub>	0.7388
$L_{ m Smooth\ L1} + L_{ m Focal\ Los}$	0.7492
$L_{ m Smooth\ L1} + L_{ m Focal\ Loss} + L_{ m Dice}$	0.7706

row shift measurements have a higher fidelity than the column and diagonal shift measurements. The lack of performance enhancement when combining column and diagonal shift data suggests that these measurements may contain overlapping information, thus not significantly improving fidelity. The highest reconstruction accuracy is achieved when training the model with the three different capacitance measurements, with the row shift data being the main contributor to the reconstruction accuracy. These findings also suggest potential areas for optimization and further research, such as improving the noise floor on column and diagonal shift readings.

Additionally, we conduct an ablation study on the impact of the loss function choice on the model's prediction accuracy. Initially, the model is trained with the smooth L1 loss function, which equally penalizes the error in the background and foreground pixels. Then, the smooth L1 loss is combined with the focal loss, which penalizes errors in the foreground pixels more than the background pixels. In the last experiment, the smooth L1 loss and the focal loss are combined with the dice loss function, which maximizes the area overlap between the prediction and the ground truth. Both the focal loss and the dice loss functions address the class-imbalance problem where foreground pixels occupy a smaller region compared to the background pixels. Table IV shows the IoU metric value for the three loss configurations when the model is trained for 20 epochs on the  $\Omega_2$  biofilm dataset. The results show that prediction accuracy increases as we incorporate more objectives in the loss function, highlighting the importance of including loss functions that address the class imbalance in

the training objective.

# VI. DISCUSSION

It is worth highlighting that the success of these experimental biofilm reconstructions does not mean that capacitance tomography is a universally solvable problem. With a planar electrode array, the magnitude of the electric field decreases rapidly at larger distances from the surface, resulting in low sensitivity to materials farther from the sensor [40]. We benefited from the thin geometry of the bacterial biofilms, which meant that a  $100\,\mu\mathrm{m}$  thick reconstruction volume was sufficient. Achieving capacitance tomography of larger or thicker objects would be more challenging and would likely require sacrificing spatial resolution.

The use of an integrated CMOS sensor [18], [26] also offered unique opportunities in this application. With a dense  $10\,\mu\mathrm{m}$  electrode pitch and  $512\times256$  array, a single recording of stacked mutual capacitance images contained millions of individual measurements, creating large datasets for statistically training and testing the reconstruction networks.

Absolute capacitance scales with electrode area, and the  $10\,\mu\mathrm{m}$  pixels of the CMOS sensor were a mixed blessing, yielding finer spatial resolution but smaller signals and shallower reconstruction depths. Working in aqueous media  $(\epsilon_r \approx 78)$  also helped to increase the capacitance signals, compared to air  $(\epsilon_r \approx 1)$ . Typical mutual capacitance values from the CMOS sensor were 1-200 femtofarads, which is possible to measure as long as some care is taken to preserve the SNR. The mutual capacitance decreases for larger electrode distances, and measurements with spatial offsets greater than 5 were near the noise floor and not used.

Labeled training and testing was made possible by alignment to 3-D confocal microscopy of the same samples without removing the biofilms from the sensor. The tomographic reconstructions were also generally simplified to be binary, only classifying the biofilm against the background. In order to work with more complex samples, the networks may need to be re-designed, and it remains to be seen how well these

networks translate across different cell types, different sample preparations, and different environments.

The media composition can also have a secondary effect on the capacitance measurements, mainly through the influence of salts and other ions on electrochemical double layers near surfaces. This effect can be complex, and it also depends on the measurement frequency [41]. In our experiments, the frequency (6.25 MHz) and the media composition were held constant, and the biofilms were mounted and sealed after growing to maturity. If the media were changing over time due to evaporation or significant metabolic activity, this could be another variable that deserves attention.

Like many deep learning systems, the tomographic networks in this work have large numbers of parameters. In order to enable training convergence and guard against over-fitting, careful design of the loss function is important (see Section III-B). One possible direction for future improvements could be to pursue closer incorporation of physics simulations with the learning network. We showed that the networks can be trained using the results of finite element simulations (e.g. Fig. 11), but the physics could be moved from being implicit in the training data, to being explicit in the training algorithms [42]. Expanded use of simulated datasets and physics-derived loss functions could help to improve future performance and broaden experimental applications, even when training data from confocal imaging is not available.

## VII. CONCLUSION

In this paper, we presented an electrical capacitance tomography (ECT) system using a CMOS sensor array for 3-D shape reconstruction of micron-scale objects. We introduced a deep learning architecture for reconstructing 3-D sample volumes from the CMOS capacitance measurements. The model was trained with an enhanced multi-objective training scheme that combines a pixel-wise loss function, a distribution-based loss function, and a region-based loss function which enhanced the 3-D shape reconstruction accuracy by 3.2% compared training only with pixel-wise loss function. We demonstrated our approach on an experimental dataset of bacterial biofilms, and were able to resolve microscopic spatial structure in the cultures. Compared to prior demonstrations of capacitance tomography or impedance tomography (Table III), this work achieves the finest spatial resolution on a platform with by far the largest number of sensing electrodes. Future work may include enhancing the 3-D shape reconstruction accuracy by using more advanced deep learning models for solving the ECT inverse problem, like diffusion models [43]. In parallel, we will broaden the scope of our training dataset to encompass a wider variety of 3-D cell cultures. Microscale ECT offers a low-cost, label-free, and non-invasive imaging technique that is suitable for a wide array of biomedical applications, including tracking the geometry of cell cultures in three dimensions.

## VIII. ACKNOWLEDGEMENT

This work was supported by the National Science Foundation under Grant No. 2027108. J.W.L. acknowledges support

from NIGMS 1R35GM142584-01 and the Burroughs Wellcome Fund. J.K.R. acknowledges the Hazeltine Innovation Award from the Brown University School of Engineering.

The models and algorithms from this work are available at https://github.com/HyBISCIS/MicroECT-3D.

#### REFERENCES

- M. Cheney, D. Isaacson, and J. C. Newell, "Electrical impedance tomography," SIAM Review, vol. 41, no. 1, pp. 85–101, 1999.
- [2] V. Tomicic and R. Cornejo, "Lung monitoring with electrical impedance tomography: technical considerations and clinical applications," *Journal* of thoracic disease, vol. 11, no. 7, p. 3122, 2019.
- [3] M. Assenheimer, O. Laver-Moskovitz, D. Malonek, D. Manor, U. Nahaliel, R. Nitzan, and A. Saad, "The t-scantm technology: electrical impedance as a diagnostic tool for breast cancer detection," *Physiological measurement*, vol. 22, no. 1, p. 1, 2001.
- [4] M. H. Choi, T.-J. Kao, D. Isaacson, G. J. Saulnier, and J. C. Newell, "A reconstruction algorithm for breast cancer imaging with electrical impedance tomography in mammography geometry," *IEEE transactions* on biomedical engineering, vol. 54, no. 4, pp. 700-710, 2007.
- [5] K. Y. Aristovich, B. C. Packham, H. Koo, G. S. D. Santos, A. McEvoy, and D. S. Holder, "Imaging fast electrical activity in the brain with electrical impedance tomography," *NeuroImage*, pp. 204–213, Jan 2016.
- [6] S. H. Arshad, J. S. Kunzika, E. K. Murphy, K. Odame, and R. J. Halter, "Towards a smart phone-based cardiac monitoring device using electrical impedance tomography," in 2015 IEEE biomedical circuits and systems conference (BioCAS), pp. 1–4, IEEE, 2015.
- [7] W. P. Taruno, M. R. Baidillah, R. I. Sulaiman, M. F. Ihsan, S. E. Fatmi, A. H. Muhtadi, F. Haryanto, and M. Aljohani, "4d brain activity scanner using electrical capacitance volume tomography (ecvt)," in 2013 IEEE 10th International Symposium on Biomedical Imaging, pp. 1006–1009, 2013.
- [8] J. Sola, A. Adler, A. Santos, G. Tusman, F. S. Sipmann, and S. H. Bohm, "Non-invasive monitoring of central blood pressure by electrical impedance tomography: first experimental evidence," *Medical & biological engineering & computing*, vol. 49, pp. 409–415, 2011.
- [9] K. Alme and S. Mylvaganam, "Electrical capacitance tomography—sensor models, design, simulations, and experimental verification," *IEEE Sensors Journal*, vol. 6, no. 5, pp. 1256–1266, 2006.
- [10] W. Fang, "A nonlinear image reconstruction algorithm for electrical capacitance tomography," *Measurement Science and Technology*, vol. 15, p. 2124, sep 2004.
- [11] W. Q. Yang and L. Peng, "Image reconstruction algorithms for electrical capacitance tomography," *Measurement Science and Technology*, vol. 14, p. R1, dec 2002.
- [12] T. C. Chandrasekera, Y. Li, J. S. Dennis, and D. J. Holland, "Total variation image reconstruction for electrical capacitance tomography," in 2012 IEEE International Conference on Imaging Systems and Techniques Proceedings, pp. 584–589, 2012.
- [13] L. Peng, H. Merkus, and B. Scarlett, "Using regularization methods for image reconstruction of electrical capacitance tomography," *Particle & Particle Systems Characterization*, vol. 17, no. 3, pp. 96–104, 2000.
- [14] J. Zheng, H. Ma, and L. Peng, "A cnn-based image reconstruction for electrical capacitance tomography," in 2019 IEEE International Conference on Imaging Systems and Techniques (IST), pp. 1–6, 2019.
- [15] J. Zheng and L. Peng, "An autoencoder-based image reconstruction for electrical capacitance tomography," *IEEE Sensors Journal*, vol. 18, no. 13, pp. 5464–5474, 2018.
- [16] H. Zhu, J. Sun, L. Xu, W. Tian, and S. Sun, "Permittivity reconstruction in electrical capacitance tomography based on visual representation of deep neural network," *IEEE Sensors Journal*, vol. 20, no. 9, pp. 4803– 4815, 2020.
- [17] G. Xinxin, T. Zenan, Q. Limin, and Z. Xiaobin, "A hybrid deep learning model for ect image reconstruction of cryogenic fluids," Flow Measurement and Instrumentation, vol. 87, p. 102228, 2022.
- [18] K. Hu, J. Incandela, X. Lian, J. W. Larkin, and J. K. Rosenstein, "A 13.1 mm 2 512× 256 multimodal CMOS array for spatiochemical imaging of bacterial biofilms," in 2022 IEEE Custom Integrated Circuits Conference (CICC), pp. 1–2, IEEE, 2022.
- [19] P. Linderholm, L. Marescot, M. H. Loke, and P. Renaud, "Cell culture imaging using microimpedance tomography," *IEEE Transactions on Biomedical Engineering*, vol. 55, no. 1, pp. 138–146, 2007.

- [20] E. J. Lee, H. Wi, A. L. McEwan, A. Farooq, H. Sohal, E. J. Woo, J. K. Seo, and T. I. Oh, "Design of a microscopic electrical impedance tomography system for 3D continuous non-destructive monitoring of tissue culture," *Biomedical engineering online*, vol. 13, pp. 1–15, 2014.
- [21] Z. Ren and W. Yang, "A miniature two-plate electrical capacitance tomography sensor," *IEEE Sensors Journal*, vol. 15, no. 5, pp. 3037– 3049, 2015.
- [22] X. F. Hor, P. L. Leow, M. S. Mohamed Ali, P. S. Chee, S. Mohammad Din, and W. P. Gooi, "Electrode configuration study for three-dimensional imaging of on-chip ect," *Engineering Research Express*, vol. 5, no. 2, p. 025003, 2023.
- [23] Y. Yang, J. Jia, S. Smith, N. Jamil, W. Gamal, and P.-O. Bagnaninchi, "A miniature electrical impedance tomography sensor and 3-d image reconstruction for cell imaging," *IEEE Sensors Journal*, vol. 17, no. 2, pp. 514–523, 2017.
- [24] Y. Yang, H. Wu, J. Jia, and P.-O. Bagnaninchi, "Scaffold-based 3-d cell culture imaging using a miniature electrical impedance tomography sensor," *IEEE Sensors Journal*, vol. 19, no. 20, pp. 9071–9080, 2019.
- [25] S. Schlafer and R. L. Meyer, "Confocal microscopy imaging of the biofilm matrix," *Journal of Microbiological Methods*, vol. 138, pp. 50– 59, 2017. What's next in microbiology methods? Emerging methods.
- [26] K. Hu, J. Ho, and J. K. Rosenstein, "Super-resolution electrochemical impedance imaging with a 512 × 256 CMOS sensor array," *IEEE Transactions on Biomedical Circuits and Systems*, vol. 16, no. 4, pp. 502–510, 2022.
- [27] K. Hu, C. E. Arcadia, and J. K. Rosenstein, "Super-resolution electrochemical impedance imaging with a 100× 100 CMOS sensor array," in 2021 IEEE Biomedical Circuits and Systems Conference (BioCAS), pp. 1–4, IEEE, 2021.
- [28] M. Abdelatty, J. Incandela, K. Hu, J. W. Larkin, S. Reda, and J. K. Rosenstein, "Microscale 3-d capacitance tomography with a cmos sensor array," in 2023 IEEE Biomedical Circuits and Systems Conference (BioCAS), pp. 1–5, 2023.
- [29] V. Dumoulin and F. Visin, "A guide to convolution arithmetic for deep learning," arXiv preprint arXiv:1603.07285, 2016.
- [30] S. Ioffe and C. Szegedy, "Batch normalization: Accelerating deep network training by reducing internal covariate shift," in *Proceedings of* the 32nd International Conference on Machine Learning (F. Bach and D. Blei, eds.), vol. 37 of *Proceedings of Machine Learning Research*, (Lille, France), pp. 448–456, PMLR, 07–09 Jul 2015.
- [31] S. A. Taghanaki, Y. Zheng, S. Kevin Zhou, B. Georgescu, P. Sharma, D. Xu, D. Comaniciu, and G. Hamarneh, "Combo loss: Handling input and output imbalance in multi-organ segmentation," *Computerized Medical Imaging and Graphics*, vol. 75, pp. 24–33, 2019.
- [32] T.-Y. Lin, P. Goyal, R. Girshick, K. He, and P. Dollar, "Focal loss for dense object detection," in *Proceedings of the IEEE International* Conference on Computer Vision (ICCV), Oct 2017.
- [33] R. Zhao, B. Qian, X. Zhang, Y. Li, R. Wei, Y. Liu, and Y. Pan, "Rethinking dice loss for medical image segmentation," in 2020 IEEE International Conference on Data Mining (ICDM), pp. 851–860, 2020.
- [34] S. Sugimoto, K.-i. Arita-Morioka, Y. Mizunoe, K. Yamanaka, and T. Ogura, "Thioflavin t as a fluorescence probe for monitoring ma metabolism at molecular and cellular levels," *Nucleic acids research*, vol. 43, no. 14, pp. e92–e92, 2015.
- [35] Z. Wang, A. C. Bovik, H. R. Sheikh, and E. P. Simoncelli, "Image quality assessment: from error visibility to structural similarity," *IEEE transactions on image processing*, vol. 13, no. 4, pp. 600–612, 2004.
- [36] B. Liu, B. Yang, C. Xu, J. Xia, M. Dai, Z. Ji, F. You, X. Dong, X. Shi, and F. Fu, "pyeit: A python based framework for electrical impedance tomography," *SoftwareX*, vol. 7, pp. 304–308, 2018.
- [37] X. Song, Y. Xu, and F. Dong, "A hybrid regularization method combining tikhonov with total variation for electrical resistance tomography," Flow Measurement and Instrumentation, vol. 46, pp. 268–275, 2015.
- [38] M. Mathieu, C. Couprie, and Y. LeCun, "Deep multi-scale video prediction beyond mean square error," in 4th International Conference on Learning Representations, ICLR 2016, San Juan, Puerto Rico, May 2-4, 2016, Conference Track Proceedings (Y. Bengio and Y. LeCun, eds.), 2016.
- [39] E. Lee, J. K. Seo, E. J. Woo, and T. Zhang, "Mathematical framework for a new microscopic electrical impedance tomography system," *Inverse Problems*, vol. 27, p. 055008, apr 2011.
- [40] Z. Ye, R. Banasiak, and M. Soleimani, "Planar array 3D electrical capacitance tomography," *Insight-Non-Destructive Testing and Condition Monitoring*, vol. 55, no. 12, pp. 675–680, 2013.

- [41] S. G. Lemay, C. Laborde, C. Renault, A. Cossettini, L. Selmi, and F. P. Widdershoven, "High-frequency nanocapacitor arrays: concept, recent developments, and outlook," *Accounts of chemical research*, vol. 49, no. 10, pp. 2355–2362, 2016.
- [42] S. Cuomo, V. S. Di Cola, F. Giampaolo, G. Rozza, M. Raissi, and F. Piccialli, "Scientific machine learning through physics-informed neural networks: Where we are and what's next," *Journal of Scientific Computing*, vol. 92, no. 3, p. 88, 2022.
- [43] H. Chung, J. Kim, M. T. Mccann, M. L. Klasky, and J. C. Ye, "Diffusion posterior sampling for general noisy inverse problems," 2023.



Manar Abdelatty recieved her B.S. in Computer Engineering from the American University in Cairo, Egypt, in 2020. She completed her Master of Science at Brown University, Providence, RI, in 2024, and is currently pursuing a Ph.D. in Electrical and Computer Engineering at the same institution. Her research focuses on applying machine learning techniques to biosensors, developing electronic design automation software, and utilizing machine learning to accelerate the hardware design process.



Joseph T. Incandela received his B.S. in Physics from the University of Santa Barbara, CA, USA, in 2019, and his M.S. degree in Physics from Boston University, MA, USA, in 2022. Currently, he is pursuing a Ph.D. in Physics at Boston University, in the field of Biophysics. His current research interests lie in probing microbial colony signaling dynamics, using microfluidics platforms with integrated biomedical electronics for in-situ biochemical measurements.



Kangping Hu (S'18) received the B.S. degree (summa cum laude) in electrical and computer engineering from Boston University, MA, USA, in 2013, the M.S. degree in electrical engineering from California Institute of Technology, CA, USA, in 2014, and the M.S. degree in computer science and Ph.D. degree in electrical engineering from Brown University, RI, USA, in 2022. He has worked as an RFIC engineer at Calterah Semiconductor, a DRAM design engineer at Micron Technology, a research intern at Meta Reality Lab, and a hardware intern at

Apple. He is currently a research engineer at Apple, Cupertino, CA, USA. His research interests include DRAM memory systems and multi-modal sensor array platforms for biosensing applications. Dr. Hu was the recipient of the IEEE Biomedical Circuits and Systems (BioCAS) Best Paper Award in 2022.



Pushkaraj Joshi received his B.E. from the University of Mumbai, India (2006), M.E. (2008) and Ph.D.(2018) from the Indian Institute of Science, India in the field of Chemical engineering. He joined General Electric Company, and worked as a Process Engineer in the area of coal/oil gasification projects. He worked as a Research Associate at the University of Cambridge, United Kingdom on self-healing circuits. He is currently a postdoctoral research associate at Brown University, Providence, RI, working in the area of bioelectronics.



Joseph W. Larkin is an Assistant Professor of Biology and Physics at Boston University in Boston, MA and a member of Boston University's Biological Design Center. He received a Ph.D. in physics from Northeastern University, an M.S. in physics from Boston University, and a B.S. in physics from Stanford University. He is a recipient of the Career Award at the Scientific Interface from the Burroughs Wellcome Fund. His current research interests include physics of bacterial communities and multicellularity in microbes.



Sherief Reda (Fellow, IEEE) received his B.Sc. and M.Sc. degrees from Ain Shams University, Cairo, Egypt, and his Ph.D. in Computer Science and Engineering from the University of California, San Diego. In 2006, he joined the Electrical and Computer Engineering Group at Brown University, Providence, RI, where he is currently a Professor of Engineering and Computer Science. His research interests include energy-efficient computing, deep learning for edge devices, and molecular computing. Prof. Reda is a recipient of the NSF CAREER Award

and has served as an Associate Editor for the IEEE Transactions on Computer-Aided Design of Integrated Circuits and Systems.



Jacob K. Rosenstein is an Associate Professor of Engineering at Brown University in Providence, RI. He received Sc.M. and Ph.D. degrees in electrical engineering from Columbia University, and an Sc.B in Computer Engineering from Brown University. He previously worked as a hardware systems engineer at Analog Devices Inc, and MediaTek Wireless Inc. His current research interests include biomedical electronics, mixed-signal circuit design, and chemical information systems.